

# Synergistic Crystallization and Passivation by A Single Molecular Additive for High Performance Perovskite Solar Cells

Xinyi Du<sup>a</sup>, Jing Zhang<sup>a\*</sup>, Hang Su<sup>a,b</sup>, Xu Guo<sup>a</sup>, Yingjie Hu<sup>a</sup>, Dongle Liu<sup>a</sup>, Ningyi Yuan<sup>c</sup>, Jianning Ding<sup>c</sup>, Lili Gao<sup>a\*</sup>, Shengzhong (Frank) Liu<sup>a,b\*</sup>

a. Laboratory of Applied Surface and Colloid Chemistry, Ministry of Education; Shaanxi Key Laboratory for Advanced Energy Devices; Shaanxi Engineering Lab for Advanced Energy Technology; Institute for Adv. Energy Mater.; School of Materials Science and Engineering, Shaanxi Normal University, Xi'an 710119, Shaanxi, China.

b. Dalian National Laboratory for Clean Energy; iChEM, Dalian Institute of Chemical Physics, Chinese Academy of Sciences, 457 Zhongshan Road, Dalian 116023, China.

c. School of Materials Science and Engineering, Jiangsu Collaborative Innovation Center for Photovoltaic Science and Engineering, Jiangsu Province Cultivation base for State Key Laboratory of Photovoltaic Science and Technology, Changzhou University, Changzhou 213164, China

Keywords: perovskite, solar cell, crystallization, efficiency, stability

## Abstract:

With its power conversion efficiency surpassed those of all other thin film solar cells only a few years after its invention, the perovskite solar cell has become a superstar. Controlling intermediate phase of crystallization is a key to obtain high-quality perovskite films. Herein, a single molecule additive, N, N-Dimethylimidodicarbonimidic diamide hydroiodide (DIAI), is incorporated into

This article has been accepted for publication and undergone full peer review but has not been through the copyediting, typesetting, pagination and proofreading process, which may lead to differences between this version and the [Version of Record](#). Please cite this article as [doi: 10.1002/adma.202204098](#).

This article is protected by copyright. All rights reserved.

perovskite precursor to eliminate the influence of intermediate phases. By taking advantage of interaction of DAI and DMSO, the intermediate phase FAI-PbI<sub>2</sub>-DMSO complex is eliminated, and  $\delta$ -FAPbI<sub>3</sub> is entirely converted to desired  $\alpha$ -FAPbI<sub>3</sub> during the crystallization step, resulting in enlarged grain size and improved crystalline quality. This is the first observation in solution method that FAPbI<sub>3</sub> can be obtained without intermediate phase for high-performance perovskite solar cells. Furthermore, DAI is effective at passivating surface defects, resulting in reduced defect density, increased carrier lifetime, and improved device efficiency and stability. The champion device achieved an efficiency of 24.13%. Furthermore, the bare device without any encapsulation maintains 94.1% of its initial efficiency after ambient exposure over 1000 hours. This work contributes a strategy of synergistic crystallization and passivation to directly form  $\alpha$ -FAPbI<sub>3</sub> from the precursor solution without the influence of intermediate impurities for high performance perovskite applications.

## 1. Introduction

Organic-inorganic hybrid perovskite materials have received extensive attention in the photovoltaic field due to their high optical absorption coefficient,<sup>[1]</sup> high carrier mobility,<sup>[2]</sup> low exciton binding energy,<sup>[3]</sup> long carrier diffusion length,<sup>[4]</sup> adjustable band gap,<sup>[5]</sup> and low manufacturing cost.<sup>[6]</sup> To date, the certified photoelectric conversion efficiency (PCE) for perovskite solar cells (PSCs) has reached 25.5%,<sup>[7]</sup> which makes perovskite solar cells a strong future competitor in the photovoltaic industry. FAPbI<sub>3</sub> has been widely used as the light absorber for single-junction PSCs due to its narrower bandgap and higher Shockley-Queisser limit efficiency compared with MAPbI<sub>3</sub>.<sup>[8]</sup> However, the perovskite devices based on FAPbI<sub>3</sub> polycrystalline films face the problem of phase and environmental instability.<sup>[9]</sup> The black  $\alpha$  phase easily transforms to the yellow  $\delta$  phase, which destroys the optoelectronic properties.<sup>[10]</sup> The phase instabilities are accelerated by the poor quality of the perovskite polycrystalline film, which is closely correlated with the crystallization process.<sup>[11]</sup> At present, rapid crystallization by the most-used solution method with DMF or DMSO solvent will inevitably lead to formation of a solution-complex intermediate phase, such as FAI-PbI<sub>2</sub>-DMSO, in the perovskite crystallization process.<sup>[12]</sup> However, the final product will not be pure and stable  $\alpha$ -FAPbI<sub>3</sub> after the process of high-temperature annealing because of the incomplete transformation of the intermediate phase and the nonstoichiometric components.<sup>[11a, 13]</sup> The existence of the solvent-complexing intermediate phase will lead to impurity phases, such as  $\delta$ -

FAPbI<sub>3</sub>, in the final product.<sup>[14]</sup> This process also leads to the formation of different types and large amounts of defects.<sup>[15]</sup> The defects act as non-radiative recombination centers, which results in degradation of the device performance.<sup>[16]</sup> In addition, the defects are the fast channel for ion migration and the origin of device decomposition.<sup>[14b, 17]</sup> Therefore, it is necessary to explore a controllable method to eliminate the influence of intermediate phases such as solvent coordination complexes during the film formation process and avoid the formation of impurity phases, so as to obtain the desired phase  $\alpha$ -FAPbI<sub>3</sub> in the final product.<sup>[18]</sup>

In this work, a simple and multifunctional phase-management method was developed to control the perovskite film crystallization and completely inhibit the formation of a solvent-coordinated perovskite intermediate complex for obtaining high-quality black  $\alpha$ -FAPbI<sub>3</sub> film. N, N-dimethylimidodicarbonimidic diamide hydroiodide (DIAI) was introduced into the perovskite bulk and onto the surface. During the crystallization process, the initial intermediate phase FAI-PbI<sub>2</sub>-DMSO disappeared, and a vital phase ( $\delta$ -FAPbI<sub>3</sub>) occurred instead because of the DIAI coordination with the dimethyl sulfoxide (DMSO) solvent. The  $\delta$ -FAPbI<sub>3</sub> finally entirely converted to  $\alpha$ -FAPbI<sub>3</sub> upon annealing. The detailed crystallization process was revealed by in situ x-ray diffraction (XRD) and in situ UV-Vis absorption spectra. The results showed that the addition of DIAI into the precursor solution could effectively improve the crystallization quality by inhibiting the formation of a solvent-coordinated intermediate complex. Meanwhile, the DIAI also stabilized the perovskite film as  $\alpha$ -FAPbI<sub>3</sub> phase, thereby yielding a high-efficiency and phase-stable solar cell. DIAI was also employed as the surface modification layer to passivate the defects and increase the carrier lifetime. The optimized device with DIAI in the bulk and at the surface achieved a champion efficiency of 24.13%. Moreover, after monitoring for 1000 hours in the ambient atmosphere at 25 °C and 45% humidity, the optimized device maintained over 94.1% of its initial efficiency. This result can be attributed the synergistic effects of DIAI. On the one hand, the DIAI optimized the crystallization process and stabilized the  $\alpha$ -FAPbI<sub>3</sub> phase. On the other hand, the DIAI passivated defects in the perovskite bulk and at the surface. This work takes advantage of the bulk and surface synergistic interactions and phase management to boost the device efficiency and stability.

## 2. Results and Discussion

### 2.1. Crystallization dynamics of perovskite film with DIAI

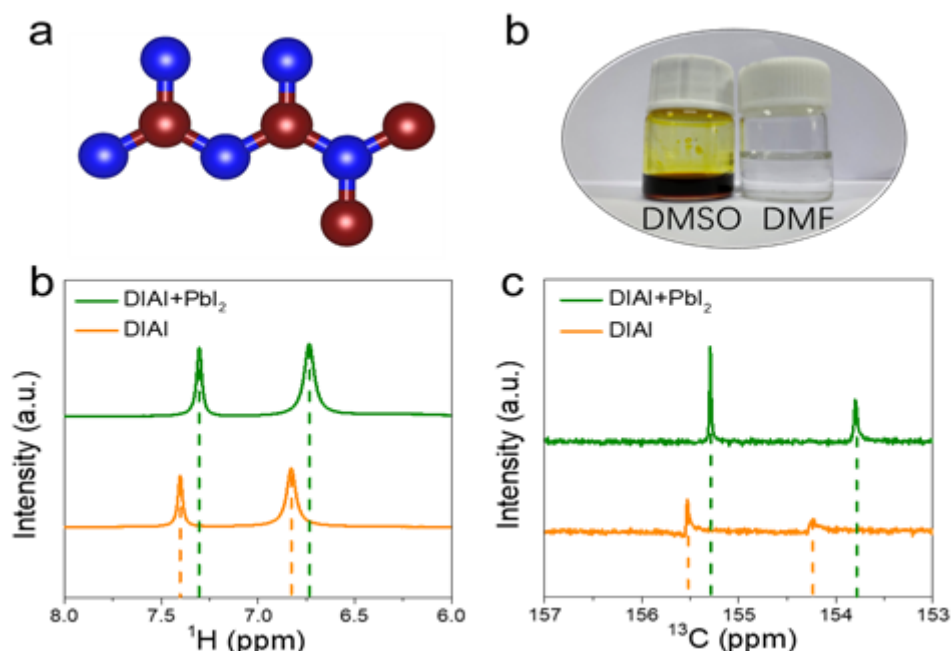


**Figure 1.** (a) The molecular structure of DIAI (the dark red represents C atoms and the blue represents N atoms) and a photograph of DIAI dissolving in DMF and DMSO, (b)  $^1\text{H}$  NMR spectra and (c)  $^{13}\text{C}$  NMR spectra of DIAI and DIAI with  $\text{PbI}_2$  in the DMSO- $d_6$  solution.

Figure 1a shows the chemical structure of DIAI. DMF and DMSO were chosen as solvents for the DIAI additive to ensure solubility and compatibility with the perovskite precursor. Video 1 shows that the solution of DIAI dissolving in DMSO was dark red, while the solution remained transparent light yellow using DMF as solvent. To reveal the intrinsic mechanism of the color difference, FTIR was conducted to research the interaction of DIAI with DMSO and DMF. The results in Figure S1 show that after DIAI is dissolved in DMSO, the typical peaks of DMSO at  $3000\text{ cm}^{-1}$  and  $1650\text{ cm}^{-1}$  assigned to C-H stretching vibration shifted to lower wavenumber, which indicated a strong interaction between DMSO and DIAI. As expected, the peaks of DIAI dissolved in DMF didn't shift. Nuclear magnetic resonance (NMR) spectroscopy was conducted to research the interaction of DIAI and  $\text{PbI}_2$ .

From the  $^1\text{H}$  NMR spectra in Figure 1b, it can be observed that the peaks of DIAI at 7.40 ppm and 6.83 ppm obviously shifted to the lower values of 7.30 ppm and 6.73 ppm after mixing the DIAI with  $\text{PbI}_2$ . Also, the same shift was observed in the  $^{13}\text{C}$  NMR spectra, as shown in Figure 1c. The peaks at 155.53 ppm and 154.23 ppm were assigned to the two C=N groups and shifted to 155.29 and 153.79 ppm, respectively, after the DIAI was mixed with  $\text{PbI}_2$ , indicating a chemical interaction between  $\text{PbI}_2$  and DIAI existed.

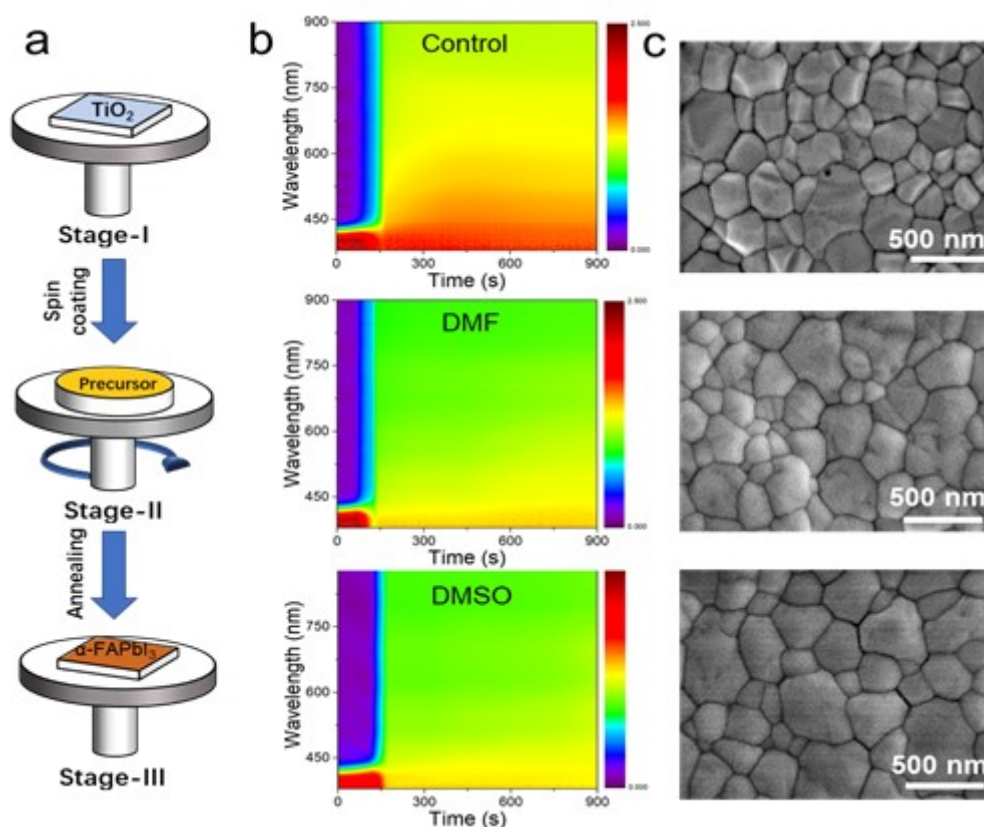


**Figure 2.** (a) Procedure for perovskite film preparation, (b) in situ UV-Vis absorption spectra in different solvents, (c) SEM images of perovskite films with and without DIAI dissolved in DMF and DMSO.

The solution procedure for preparation of the perovskite films is shown in Figure 2a and consists of three stages: dropping the precursor solution, spin-coating to form the intermediate-phase film and annealing to obtain the perovskite film. In order to clearly understand the film

formation process, we defined the control sample (without DIAI, the solvent was mixed DMSO and DMF = 4:1), DMF sample (with DIAI dissolved in DMF), and DMSO sample (with DIAI dissolved in DMSO). The dynamic film crystallization process of perovskite films with and without DIAI was detected by in-situ UV-Vis absorption measurement, and the result are shown in Figure 2b. The absorption intensity at 400 nm was strong throughout the whole annealing time for the control film. The intensity from 450 to 800 nm increased gradually with rising temperature, indicating the formation of black perovskite. With the addition of DIAI, the red region below 425 nm changed to yellow after 160 s, while the absorption of the perovskite from 450 nm to 800 nm increased simultaneously. This phenomenon is representative of perovskite crystallization, which signals the transformation from the intermediate to perovskite phase. SEM images showed that with DIAI, the perovskite crystal grains were slightly larger than those of the control (Figure 2c). The intermediate phase was observed in the XRD patterns in Figure 3a. For the control film, there are two main peaks at  $6.5^\circ$  and  $8.0^\circ$ , which are assigned to the intermediate phase. However, there are no peaks below  $10^\circ$  and the peak of  $\delta$ -FAPbI<sub>3</sub> at  $11.7^\circ$  is predominant with added DIAI. The results proved that the DIAI additive changed the intermediate phase and might affect the pathway of the chemical reaction from precursor to final solid film.

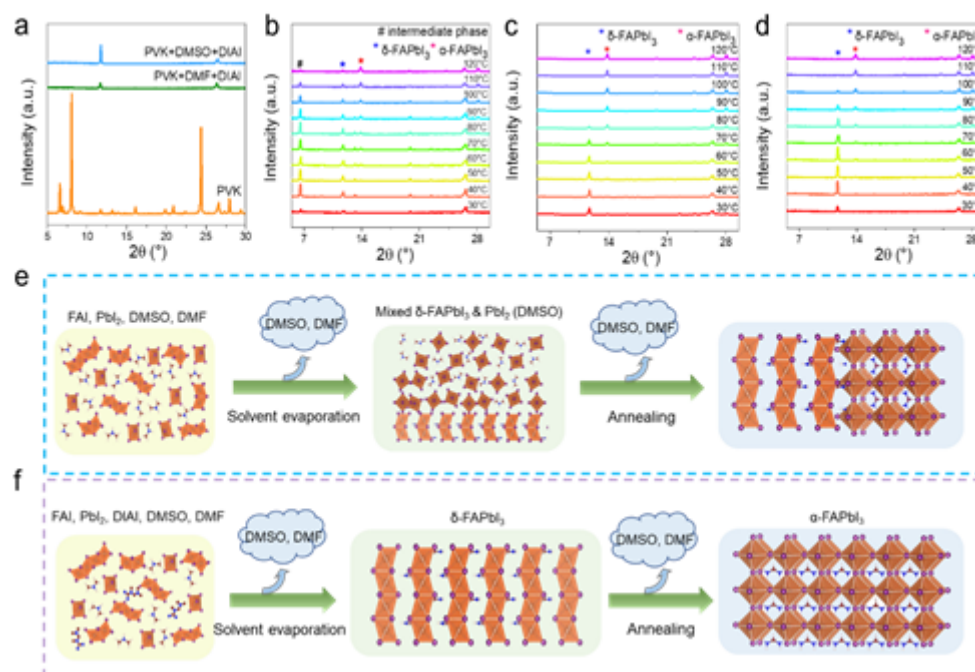


**Figure 3.** (a) XRD patterns of pristine perovskite precursor film without antisolvent dripping, with 1% DIAI dissolved in DMF and DMSO. In situ XRD patterns of the perovskite precursor films without antisolvent dripping: (b) control, (c) with DIAI dissolved in DMF, (d) with DIAI dissolved in DMSO. The crystallization process of the perovskite films: (e) control and (f) with DIAI.

To gain further insight into the film crystallization process, in situ XRD measurements were conducted. At room temperature ( $\sim 30^\circ\text{C}$ ), there's a diffraction peak below  $10^\circ$  for the control perovskite film, which could be indexed to the  $\text{FAI}\cdot\text{DMSO}\cdot\text{PbI}_2$  intermediate phase (see Figure 3b). With rising temperature, the intermediate phase transformed to  $\delta\text{-FAPbI}_3$  below  $70^\circ\text{C}$ . The  $\delta\text{-FAPbI}_3$  further converted to  $\alpha\text{-FAPbI}_3$  when the temperature exceeded  $70^\circ\text{C}$ ; however,  $\delta\text{-FAPbI}_3$  still existed even at  $120^\circ\text{C}$ , which indicates the transformation from  $\delta\text{-FAPbI}_3$  to  $\alpha\text{-FAPbI}_3$  phase was incomplete. With DIAI, the peak of the intermediate phase can't be found, and there's only one peak at  $11.7^\circ$  of  $\delta\text{-FAPbI}_3$  when the temperature is below  $70^\circ\text{C}$ . With increasing temperature, the  $\delta\text{-FAPbI}_3$  changes phase to  $\alpha\text{-FAPbI}_3$ . The phase transformation finished at  $90^\circ\text{C}$  for the DMF solution (see Figure 3c) and  $110^\circ\text{C}$  for the DMSO solution (see Figure 3d). These results indicated that DMSO was a terrific solvent for DIAI and the additive was beneficial for phase stability of  $\alpha\text{-FAPbI}_3$ , which is beneficial for highly efficient and stable perovskite solar cells. The process discussed above is vividly summarized in Figure 3e and f. DIAI can suppress the formation of the intermediate phase by complexing with DMSO; meanwhile, the complex also promotes the phase transformation.

The dynamics of the formation can also be proven by the ultrafast photo-excited carrier dynamics in the DMSO and DMF samples. We conducted femtosecond (fs) transient absorption spectroscopy (TAS) with photoexcitation at 480 nm on control and modified perovskite films, and the results shown in Figure S2. The contour plots of the TAS spectra of the control and DIAI-modified perovskite films all exhibited a distinct ground-state bleaching (GSB) peak at  $\sim 800\text{ nm}$ , which is in line with the absorption onset of the 3D perovskite film, and its intensity can reflect the photo-induced carrier populations in the conduction and valence bands of the perovskite.<sup>60, 61</sup> It is noticeable that the TAS spectrum of the DIAI-modified perovskite film displays an obvious GSB peak centered at  $\sim 500\text{ nm}$ , which matches the photoluminescence (PL) peaks of  $\delta\text{-FAPbI}_3$  (Figure S3). PL measurements during the drying process were conducted on the perovskite films with and without



DIAI. The fluorescence peaks present at  $\sim 500$  nm and  $\sim 800$  nm illustrate the coexistence of  $\delta$ -FAPbI<sub>3</sub> and  $\alpha$ -FAPbI<sub>3</sub>. Due to the evaporation of solvent, the control sample changed from  $\delta$ -FAPbI<sub>3</sub> to  $\alpha$ -FAPbI<sub>3</sub> in a short period of time and quickly transformed back to  $\delta$ -FAPbI<sub>3</sub>, as shown in Figure S3a. After 18 min of tracking, it was found that the films with added DIAI, especially the DMSO sample, showed a slower transition rate than that without additives. The sample modified with DIAI in DMF solution turned slowly from  $\delta$ -FAPbI<sub>3</sub> to  $\alpha$ -FAPbI<sub>3</sub> (Figure S3b), and the sample with DIAI dissolved in DMSO remained  $\delta$ -FAPbI<sub>3</sub> (Figure S3c) as a result of the high boiling point and low volatility of DMSO. The results suggested that DIAI would slow the crystallization rate of the perovskite film and increase the film quality.

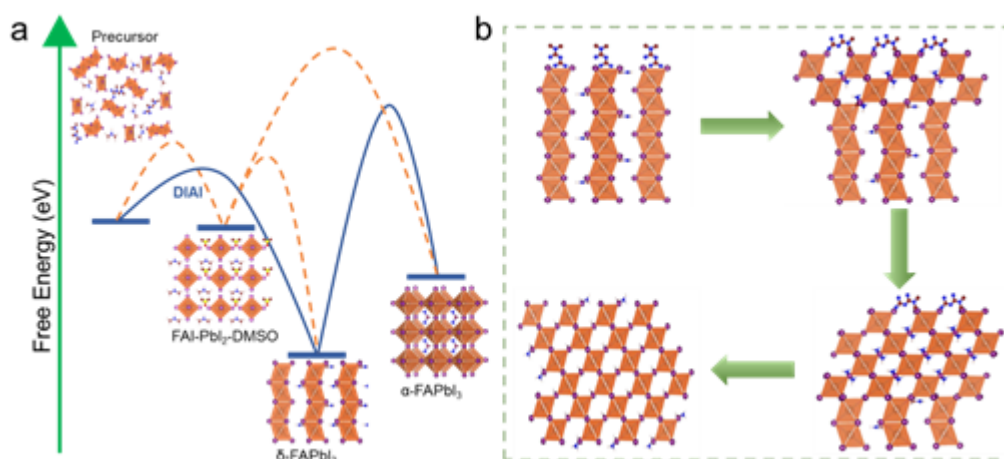


**Figure 4.** (a) Free-energy for the formation of FAPbI<sub>3</sub> perovskites with DIAI. (b) Schematic diagram of crystal growth with DIAI.

As  $\alpha$ -FAPbI<sub>3</sub> is known to be a high-temperature stable phase, the conversion energy from the intermediate phase to  $\alpha$ -FAPbI<sub>3</sub> is high, which results in the need for high-temperature annealing and causes a rapid and uncontrollable transformation from the DMSO-coordinated complexes to both  $\alpha$ -FAPbI<sub>3</sub> and  $\delta$ -FAPbI<sub>3</sub>. However, when DIAI is added, the intermediate phase is restrained and the energy consumption for DMSO-coordinated complexes dissociate on is eliminated, and thus the formation energy of  $\alpha$ -FAPbI<sub>3</sub> from  $\delta$ -FAPbI<sub>3</sub> is dramatically decreased (Figure 4a). In addition, the



chemical component is more controllable with  $\delta$ -FAPbI<sub>3</sub> as a transition phase to obtain stoichiometric  $\alpha$ -FAPbI<sub>3</sub>.

Due to the large molecular size of DIAI, it is impossible that DIA ions embed into the perovskite lattice. A possible molecular mechanism for DIAI additive changing the reaction path from the precursor to desired  $\alpha$ -FAPbI<sub>3</sub> is displayed in Figure 4b. It shows that DIA ions graft onto the surface of room-temperature stable  $\delta$ -FAPbI<sub>3</sub> by binding to Pb<sup>2+</sup>. This structure is destroyed by the annealing process, and with energy absorption, the top layer of face-sharing octahedra change to the corner-sharing octahedra of  $\alpha$ -FAPbI<sub>3</sub>. Then the first layer acts as a template and induces the transition of deeper perovskite from  $\delta$ - to  $\alpha$ -FAPbI<sub>3</sub>, thus resulting in controllable and complete phase transformation.

It is well-known that  $\alpha$ -FAPbI<sub>3</sub> is unstable at room temperature and will transform to  $\delta$ -FAPbI<sub>3</sub><sup>[11a, 19]</sup>. At room temperature, the energy barrier is readily overcome and the FAPbI<sub>3</sub> would undergoes a phase transition from the black  $\alpha$ -phase to the photoinactive  $\delta$ -phase. We traced the stability of perovskite with and without DIAI by XRD in 25 ° C and 45% RH. After 36 days of tracking, the films with added DIAI, especially the DMSO sample, were much more stable than that without additive. For the control sample in Figure S4a, the peaks of  $\alpha$ -FAPbI<sub>3</sub> almost disappear, while the strong  $\delta$ -FAPbI<sub>3</sub> peak can be clearly observed. The sample modified with DIAI dissolved in DMF had a small amount of phase reversal (Figure S4b). Only the sample with DMSO-dissolved DIAI as an additive remained  $\alpha$ -FAPbI<sub>3</sub> (Figure S4c).

## 2.2. Combined modification of bulk addition and surface passivation

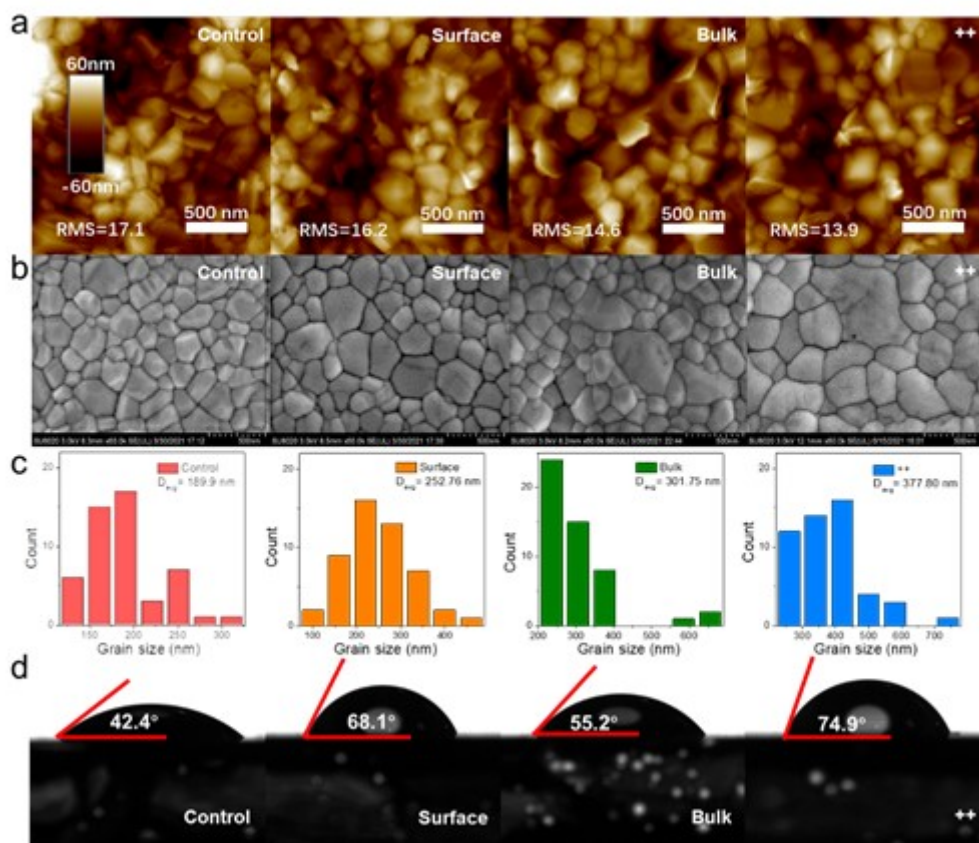


**Figure 5.** The morphology of perovskite films with and without DIAI, (a) AFM images, (b) SEM images, (c) grain size distributions, and (d) contact angles. (bulk and surface double-treated is marked as ++, bulk-passivated is marked as bulk, and surface-modified is marked as surface)

Because of the ionic salt property of DIAI and to further improve the quality of perovskite films, DIAI was also employed on the film surface to passivate defects. Atomic force microscopy (AFM) images are depicted in Figure 5a. It was found that the DIAI bulk and surface double-treated (marked as ++), bulk-passivated (marked as bulk), and surface-modified (marked as surface) perovskite films exhibited smaller roughness with root mean square values of 13.9, 14.6, 16.2 nm, respectively, compared with 21.61 nm for the control film, which was beneficial to the contact between the hole transport layer and perovskite layer and thus facilitated carrier extraction. Figure 5b shows the top-view SEM images of the perovskite films. All samples formed dense films without pinholes, and the grain size of perovskite films with DIAI in the bulk and/or on the surface enlarged slightly. As shown

in Figure 5c, the grain size of the sample with bulk additive was significantly increased to 301.75 nm, while the final average grain size of the ++ sample reached 377.80 nm, which was nearly double that of the control sample (189.9 nm). The larger grain size may be attributed to better management of crystallization and solution-processed secondary growth of surface guanidyl as reported by Luo et al.<sup>[20]</sup> Then, the contact angle tests exhibited that with DIAI in the bulk and deposited on the surface, films have better hydrophobicity, and the ++ film had the best hydrophobicity as a result of the superposition of the bulk and surface effects.

To analyze the effect of DIAI on the optical and photovoltaic performance of perovskite films, the absorption spectra of the perovskite films were first acquired. As shown in Figure S5a, the absorption intensity at 300-600 nm of perovskite films was enhanced by DIAI modification due to the enhanced perovskite film quality. Tauc plots were created from UV-Vis absorption data, and the bandgap was the same with or without adding DIAI (Figure S5b). The absorption coefficient at different wavelengths was shown in Figure S5c.

Figure S6 shows the X-ray photoelectron spectroscopy (XPS) spectra of the control and DIAI-modified perovskite films on FTO glass. The interaction between DIAI and the perovskite film could be confirmed by a shift in the binding energy of the  $\text{Pb}^{2+}$  in Figure S6a, especially with the bulk addition. As Figure S14 shows the DIAI contains both electron-rich and electron-poor moieties that can passivate positive and negative defects in perovskite thin film bulk and surface due to the interesting molecular electrostatic potential.<sup>[21]</sup> Ultraviolet photoelectron spectroscopy (UPS) was used to measure the band position with and without the DIAI treatment. As shown in Figure S7 and S8, with passivation by DIAI, the band aligned better with the interface layers than for the control, which was beneficial for carrier extraction.

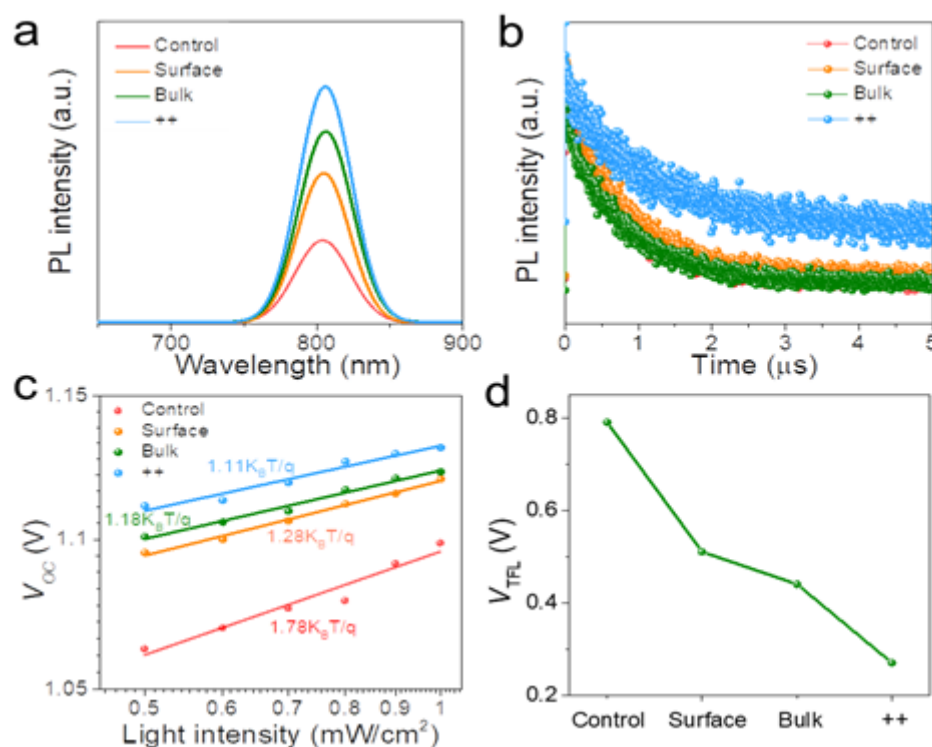


**Figure 6.** (a) Steady-state PL spectra, (b) TRPL spectra, (c) light-intensity-dependent  $V_{oc}$ , and (d) VTFL measured by the SCLC method of control, surface, bulk and ++ samples. All tested on glass.

As shown in Figure 6a, the PL spectra indicated that the DIAI-modified perovskite film presented a strong emission peak intensity. We found that the PL intensities were obviously increased by DIAI treatment, especially for the ++ sample, which indicates the nonradiative recombination in the perovskite films can be largely suppressed. Time-resolved photoluminescence (TRPL) spectra (Figure 6b) further illustrated that the double-treated perovskite films presented a longer average carrier lifetime of  $\tau = 1074.70$  ns than  $\tau = 750.00$  ns for the control film, and the specific decay times,  $\tau_1$  and  $\tau_2$ , are shown in Table S1. Improved PL intensity and prolonged carrier lifetime suggested that the defects in perovskite films could be effectively passivated by DIAI molecules.

The device response under different light intensities was tested to explore the defect passivation by DIAI. The relationship between  $V_{oc}$  and light intensity is plotted in Figure 6c, where it can be seen that the control device showed a slope of  $1.78 K_B T/q$ , while the DIAI-treated devices showed much smaller slopes ( $1.11 K_B T/q$  for double-treated,  $1.18 K_B T/q$  for bulk and  $1.28 K_B T/q$  for surface), where  $K_B$  is the Boltzmann constant,  $T$  is temperature and  $q$  is the electric charge. It is known that deviation of the slope from  $K_B T/q$  reflects defect-assisted recombination in the devices. These results further confirmed that the nonradiative recombination has largely been suppressed.

To elucidate the reduced trap-assisted recombination with DIAI modification, we determined the electron trap density ( $N_t$ ) of the perovskite films from the  $J$ - $V$  curves of electron-only devices (Figure 6d and Figure S9),  $N_t = (2\epsilon\epsilon_0 V_{TFL})/(eL^2)$  is used to quantitatively evaluate the defect density. The  $\epsilon_0$ ,  $\epsilon$ ,  $e$ , and  $L$  represent the permittivity of vacuum, relative dielectric constant of the perovskite, electron charge, and thickness of the perovskite thin film, respectively, the values of the voltage ( $V_{TFL}$ ) is the applied voltage at the kink point, namely the onset voltage of the trap-filled limit region. The  $V_{TFL}$  of the control, surface, bulk and ++ films were 0.793, 0.514, 0.443 and 0.271 V, with consequent calculated trap densities of  $1.99 \times 10^{16}$ ,  $1.29 \times 10^{16}$ ,  $1.11 \times 10^{16}$  and  $6.80 \times 10^{15} \text{ cm}^{-3}$ , respectively, which indicated that DIAI could effectively passivate the defects and the reduce defect density, in good agreement with the PL, TRPL and  $V_{oc}$  results discussed above.

### 2.3. Device performance

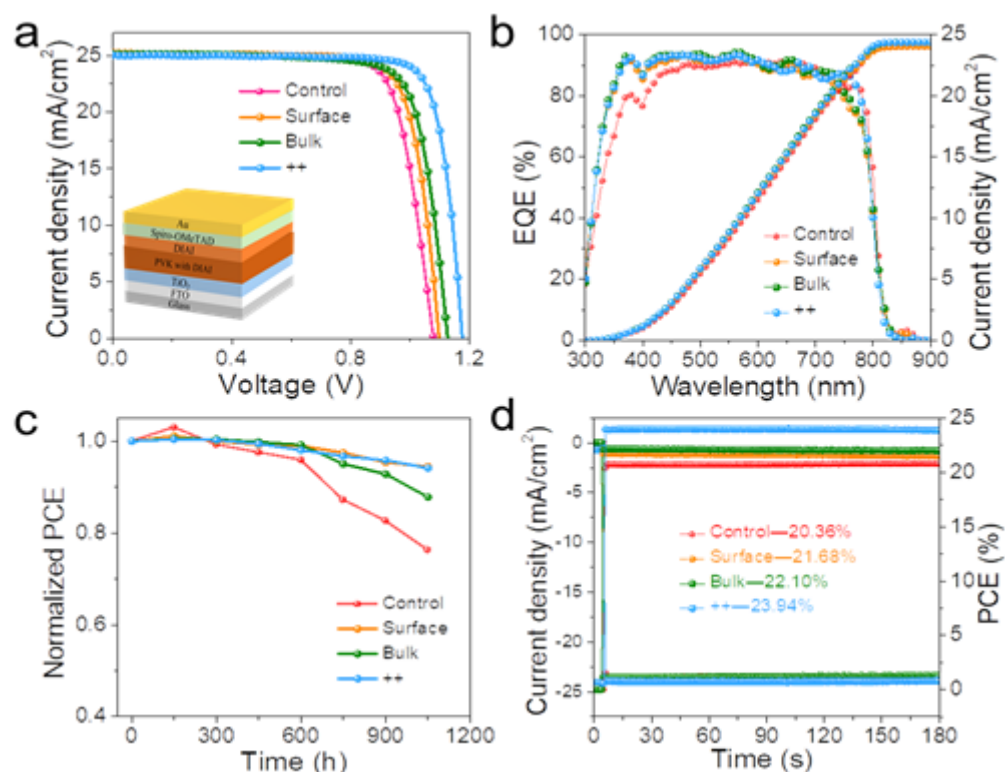


**Figure 7.** Device performance, (a)  $J$ - $V$  curves of devices employing DIAI, (b) EQE and integrated  $J_{sc}$ , (c) steady-state output current and efficiency, and (d) PCE evolution of the unencapsulated device under 45% RH at 25 °C in dark ambient conditions.

Thanks to the great defect passivation and crystallization management, solar cells with the planar device structure were constructed to obtain higher PCE, as shown in Figure 7a. DIAI was dissolved in the precursor with DMSO as the solvent for bulk and surface modification of the perovskite films. The typical  $J$ - $V$  curves of devices with and without DIAI treatment are shown in Figure 7a and Table S2. The  $V_{oc}$  of devices with DIAI addition substantially increased compared with the control device. The control device showed a PCE of 20.72% ( $J_{sc}$  of  $25.14 \text{ mA cm}^{-2}$ ,  $V_{oc}$  of 1.060V, and FF of 77.70%). The surface-modified device produced a PCE of 21.83% ( $J_{sc}$  of  $25.22 \text{ mA cm}^{-2}$ ,  $V_{oc}$  of 1.098 V, and FF of 78.84%). The bulk-passivated device achieved a PCE of 22.13% ( $J_{sc}$  of  $25.13 \text{ mA cm}^{-2}$ ,  $V_{oc}$  of 1.126 V, and FF of 78.14%). Finally, the device with bulk and surface double treatment obtained a PCE of 24.13% with  $J_{sc}$  of  $25.06 \text{ mA cm}^{-2}$ ,  $V_{oc}$  of 1.176 V, and FF of 81.89%. The dark  $J$ - $V$

cures are shown in Figure S10. The hysteresis index (HI) was defined as  $(PCE_{reverse} - PCE_{forward})/PCE_{reverse} * 100\%$ , and the hysteresis was evidently retarded with the incorporation of DIAI, as shown in Figure S11. The improvement of device performance can be attributed to the reduction of defects at the surface and in the bulk. Figure 7b shows the external quantum efficiency (EQE), and the integrated  $J_{sc}$  were 24.22, 24.04, 24.36, and 24.36  $\text{mA cm}^{-2}$ , for the control, surface, bulk and ++ devices, respectively, which matched well with the  $J_{sc}$  obtained from the  $J$ - $V$  curves. Figure 7c shows the stabilized photocurrent density and PCEs measured near the maximum power points for 180 s with applied bias voltages of 1.00 V, 0.94 V, 0.92 V and 0.88 V for the ++, bulk, surface, and control samples, respectively. All devices quickly responded when light was on, and the current density remained at 23.13, 23.57, 23.52 and 23.94  $\text{mA cm}^{-2}$  for the control, surface, bulk and ++ devices, respectively, with corresponding PCEs of 20.36%, 21.68%, 22.10% and 23.94%. In addition, the introduction of DIAI into perovskite solar cells significantly improved the devices' ambient stability. The unencapsulated stability of devices was tested at a temperature of 25 °C and humidity of 45% in the air environment for 1000 hours. The results (Figure 7d) revealed an enhanced stability for DIAI modification no matter whether at the surface or in the bulk. The control device exhibited the worst stability and only maintained 76% of its initial efficiency, while the bulk device, surface device and ++ device retained 88%, 94% and 94%, respectively, of their original efficiencies. The improved stability may be attributed to the following effects: 1) The enhancement of film hydrophobicity, confirmed by the increased water contact angle (Figure 5d) from 42.4° to 74.9° for better water-resistance; 2) Effective defect passivation reduces the active sites of degradation. In addition, we also tracked the devices light stability in a  $\text{N}_2$ -filled glovebox under continuous 1-sun illumination at 45 °C, the results are shown in Figure S12. The bulk device, surface device and ++ device retained 95%, 93% and 97% of its initial efficiency, which much well than the control device maintaining 77% original efficiency. Briefly, the DIAI modification not only helped to eliminate the hysteresis and improve efficiency, but also improved the device stability. The statistics of the  $V_{oc}$ ,  $J_{sc}$ , FF and PCE for 50 solar cells of each type confirmed the reproducibility of device performance, and the DIAI treatment undoubtedly improved  $V_{oc}$  because of the suppression of nonradiative recombination, and thus enhanced the performance of PSCs (Figure S13).



### 3. Conclusion

By simultaneous control of the intermediate phase during crystallization of the perovskite film and surface passivation using the molecule DIAI with multiple functional groups, it is found that DIAI effectively transforms the  $\delta$ -FAPbI<sub>3</sub> to  $\alpha$ -FAPbI<sub>3</sub> without any observable intermediate phase during the perovskite film formation, leading to a more stable  $\alpha$ -FAPbI<sub>3</sub> phase with improved defect passivation. Due to the improved perovskite film quality, the PL intensity is enhanced, the carrier lifetime prolonged, and the defect density reduced. This strategy enabled us to obtain an impressive device PCE as high as 24.13% with negligible hysteresis. The bare device without any encapsulation maintains 94.1% of its initial efficiency after ambient exposure for over 1000 hours. This work opens a new avenue to stabilize  $\alpha$ -FAPbI<sub>3</sub> for high-efficiency, stable PSCs.

### 4. Experimental Section

#### Materials

Dimethylsulfoxide (DMSO, 99.9%) and N, N-dimethylformamide (DMF, 99.8%) were purchased from Aladdin Biochemical Technology Co., Ltd. 4-tert-butylpyridine (t-BP), ethyl acetate (EAC), isopropanol (IPA), hydriodic acid (57%, in water), and lithium bis (trifluoromethylsulfonyl) imide salt (Li-TFSI) were purchased from Sigma-Aldrich. Lead (II) iodide (PbI<sub>2</sub>, 99.999%), formamidinium iodide (FAI, 99.9%), methylammonium iodide (MAI, 99.9%), methylammonium bromide (MABr, 99.9%), Cesium iodide (CsI, 99.9%), and spiro-OMeTAD were purchased from Liaoning Youxuan New Energy Technology Co., Ltd. N, N-Dimethylimidodicarbonimidic diamide (DIA) was purchased from Shanghai Bidepharm Technology Co., Ltd. All materials were used as received.

#### Material synthesis

DIA (1 g) was dissolved in 3.5755 g hydriodic acid (HI). The solution was stirred in a freezer at 0 °C for six hours followed by rotary steaming at 60 °C for one hour. The obtained product was dissolved in

ethanol and washed with ether, and the process was repeated three times. Finally, the white powder product (DIAI) was dried in a vacuum drying oven at 60 °C for eight hours.

### Solution preparation

Perovskite precursor solution was obtained by combining FAI, MABr, CsI and  $\text{PbI}_2$  (0.1755 g, 0.0131 g, 0.0162 g, 0.5532 g, respectively) in 1 mL mixed solvent (DMF: DMSO = 4:1),  $\text{Cs}_{0.05}\text{FA}_{0.85}\text{MA}_{0.10}\text{Pb}(\text{I}_{0.97}\text{Br}_{0.03})_3$ . Additives (DIAI) were added into the solution at 1% volume ratio (pre-dissolved as a 1.0 M stock solution in DMF or DMSO). DIAI (surface) solution: DIAI (0.0010 g) was dissolved in 1 mL isopropanol (IPA). For Spiro-OMeTAD solution, 90 mg Spiro-OMeTAD, 22  $\mu\text{L}$  Li-TFSI solution (520 mg in 1 mL acetonitrile) and 36  $\mu\text{L}$  4-tert-butylpyridine were dissolved in 1 mL chlorobenzene (CB). The solutions were stirred at room temperature for 12 h and then filtered through a 0.45- $\mu\text{m}$  syringe filter.

### Device fabrication

Fluorine-doped tin oxide (FTO) glass was chosen as the substrate. The FTO was cleaned by ultrasonication sequentially in cleaning concentrate, deionized water, and ethanol for 30 min. Then the cleaned substrate was dried by nitrogen flow and treated in a UV-ozone cleaner for 15 min. The  $\text{TiO}_2$  electron-transfer layer was prepared by chemical-bath deposition on FTO/glass substrate as reported previously.<sup>[22]</sup> Firstly, the cleaned FTO/glass substrate was treated by UV-ozone cleaner for 10 min. Then the substrate was placed in the  $\text{TiCl}_4$  aqueous solution with 0.2 M at 70 °C for 60 min, then the substrate was washed by deionized water and ethyl alcohol alternately three times. And then the substrate was annealed at 200 °C for 30 min in air and treated in UV-ozone for 20 min to enhance the wettability. Approximately 80  $\mu\text{L}$  perovskite precursor was dropped onto the  $\text{TiO}_2$ /FTO/glass substrates, and the anti-solution method was employed to form perovskite films with ethyl acetate (EAC) as the anti-solvent. The solution was spin-coated at 2000 rpm for 10 s, and then at 6000 rpm for 30 s. Ten seconds before the end of the step, 250  $\mu\text{L}$  of EAC was quickly dropped onto the surface. Then the film was annealed at 120 °C for 20 min. For surface treatment, 70  $\mu\text{L}$  DIAI

solution was dropped onto the surface at 7000 rpm for 30 s. Then, 50  $\mu\text{L}$  Spiro-OMeTAD solution was spin-coated at 5000 rpm for 30 s to form the hole-transfer layer. The gold electrode ( $\sim 80$  nm) was thermally evaporated onto the surface of the Spiro-OMeTAD through a shadow mask, and the active area is  $0.09\text{ cm}^2$ .

### Device characterization

XRD patterns were acquired using a Bruker D8 GADDS Diffractometer with  $\text{Cu K}\alpha$  ( $\lambda = 1.54\text{ \AA}$ ) radiation. The surface morphologies of the perovskite films and cross-sectional images of the PSCs were obtained using a field-emission SEM (HITACHI, SU-8020). The AFM images were captured using a Bruker Dimension Icon instrument. NMR was performed using a JNM-ECZ400S/L1 with a frequency of 400 MHz, and deuterated DMSO was used as the solvent. Water contact angle measurements were performed on an OCA20 instrument (Data-physics). XPS and UPS analyses were performed using a photoelectron spectrometer (ESCALAB 250Xi, Thermo Fisher Scientific). Absorption spectra of perovskite films prepared on glass were obtained on a UV-vis NIR spectrophotometer (Ocean Optics Instrument). In-situ UV-Vis absorption spectra were recorded on an F20 spectrometer (Filmetrics, Inc.). Transient absorption (TA) measurements were performed using a commercial TA system (Time-Tech Spectra, LLC). Femtosecond pump-probe TA measurements were performed at an appropriate power density ( $0.2\text{ mW/cm}^2$ ). The pump pulse with a wavelength of 480 nm and duration of 290 fs generated via a second harmonic generator (SHG) was used to excite all the samples, and the probe beam (from 480 to 850 nm) was detected by a high-speed spectrometer. PL spectra were investigated using an Edinburgh Instruments Ltd. FLS980 spectrometer under 510 nm wavelength excitation, and TRPL spectra were measured using a PicoQuant FluoQuant 300. The sample of PL and TRPL were prepared on glass. J-V characteristics of the hybrid PSCs were measured using a solar simulator (AM 1.5G, SAN-EIELECTRIC XES-40S2-CE) calibrated using a standard silicon solar cell certified at 2021.02.03. Approximately 50 devices were fabricated and measured independently under each experimental condition to confirm the reproducibility of the result and to obtain the statistical data of the photovoltaic parameters. The J-V curves were measured in the forward ( $-0.1$  to  $1.5\text{ V}$ ) and reverse ( $1.5$  to  $-0.1\text{ V}$ ) scan directions at room temperature and 20-30%

humidity. The scan speed is 320 mV/s and delay time is 10 ms. EQE spectra of the PSCs were measured using a Q Test Station 500TI system (Enli Technology Co., Ltd). The monochromatic light intensity was adjusted using a reference silicon detector.

### Statistical Analysis

All statistics analyses were performed with Origin 9.1. The data obtained from NMR, FTIR, in situ UV-vis, XRD, TAS, SEM, AFM, UV-vis, PL, TRPL, contact angles, XPS, UPS, *J-V*, *I-T* and EQE were the original data without normalization. The other data were obtained by transferring corresponding original data according to the calculation formula. Linear fittings were applied to SCLC (Figure S9) and Voc versus light intensity plots (Figure 6c). The grain statistics data of SEM were calculated using the Nano Measurer software. Biexponential decay function was applied to TRPL decays to infer the carrier extraction/recombination dynamics. The statistical distribution data of PCE, *J*<sub>sc</sub>, Voc, and FF were got from 50 independent devices.

### Supporting Information

Supporting Information is available from the Wiley Online Library or from the author.

### Acknowledgements

The authors acknowledge funding support from the National Natural Science Foundation of China (62004121 and 62174103), the Fundamental Research Funds for the Central Universities (GK202103107 and GK202103109), and the China Postdoctoral Science Foundation (2021M692002).

Received: ((will be filled in by the editorial staff))

Revised: ((will be filled in by the editorial staff))

Published online: ((will be filled in by the editorial staff))

## References

- [1] a) S. De Wolf, J. Holovsky, S. J. Moon, P. Loper, B. Niesen, M. Ledinsky, F. J. Haug, J. H. Yum, C. Ballif, *J. Phys. Chem. Lett.* **2014**, 5, 1035; b) M. G. Ju, M. Chen, Y. Y. Zhou, J. Dai, L. Ma, N. P. Padture, X. C. Zeng, *Joule* **2018**, 2, 1231.
- [2] a) L. M. Herz, *ACS Energy Lett.* **2017**, 2, 1539; b) J. Zhang, J. J. Qin, M. S. Wang, Y. J. Bai, H. Zou, J. K. Keum, R. M. Tao, H. X. Xu, H. M. Yu, S. Haacke, B. Hu, *Joule* **2019**, 3, 3061.
- [3] a) S. D. Stranks, G. E. Eperon, G. Grancini, C. Menelaou, M. J. P. Alcocer, T. Leijtens, L. M. Herz, A. Petrozza, H. J. Snaith, *Science* **2013**, 342, 341; b) S. Bai, P. Da, C. Li, Z. Wang, Z. Yuan, F. Fu, M. Kawecki, X. Liu, N. Sakai, J. T.-W. Wang, S. Huettnner, S. Buecheler, M. Fahlman, F. Gao, H. J. Snaith, *Nature* **2019**, 571, 245.
- [4] a) M. Vasilopoulou, A. Fakharuddin, A. G. Coutsolelos, P. Falaras, P. Argitis, A. R. B. Yusoff, M. K. Nazeeruddin, *Chem. Soc. Rev.* **2020**, 49, 4496; b) Y. C. Kim, N. J. Jeon, J. H. Noh, W. S. Yang, J. Seo, J. S. Yun, A. Ho-Baillie, S. Huang, M. A. Green, J. Seidel, T. K. Ahn, S. I. Seok, *Advanced Energy Materials* **2016**, 6, 1502104.
- [5] a) G. E. Eperon, S. D. Stranks, C. Menelaou, M. B. Johnston, L. M. Herz, H. J. Snaith, *Energy & Environmental Science* **2014**, 7, 982; b) L. Gao, F. Zhang, C. Xiao, X. Chen, B. W. Larson, J. J. Berry, K. Zhu, *Advanced Functional Materials* **2019**, 29, 1901652.
- [6] a) K. Liu, Q. Liang, M. C. Qin, D. Shen, H. Yin, Z. W. Ren, Y. K. Zhang, H. K. Zhang, P. W. K. Fong, Z. H. Wu, J. M. Huang, J. H. Hao, Z. J. Zheng, S. K. So, C. S. Lee, X. H. Lu, G. Li, *Joule* **2020**, 4, 2404; b) I. Mathews, S. Sofia, E. Ma, J. Jean, H. S. Laine, S. C. Siah, T. Buonassisi, I. M. Peters, *Joule* **2020**, 4, 822.
- [7] a) J. Jeong, M. Kim, J. Seo, H. Z. Lu, P. Ahlawat, A. Mishra, Y. G. Yang, M. A. Hope, F. T. Eickemeyer, M. Kim, Y. J. Yoon, I. W. Choi, B. P. Darwich, S. J. Choi, Y. Jo, J. H. Lee, B. Walker, S. M. Zakeeruddin, L. Emsley, U. Rothlisberger, A. Hagfeldt, D. S. Kim, M. Gratzel, J. Y. Kim, *Nature*, 16; b) L. K. Ono, Y. B. Qi, S. Z. Liu, *Joule* **2018**, 2, 1961; c) H. Min, D. Y. Lee, J. Kim, G. Kim, K. S. Lee, J. Kim, M. J. Paik, Y. K. Kim, K. S. Kim, M. G. Kim, T. J. Shin, S. Il Seok, *Nature* **2021**, 598, 444.
- [8] a) M. Jeong, I. W. Choi, E. M. Go, Y. Cho, M. Kim, B. Lee, S. Jeong, Y. Jo, H. W. Choi, J. Lee, J.-H. Bae, S. K. Kwak, D. S. Kim, C. Yang, *Science* **2020**, 369, 1615; b) J. J. Yoo, G. Seo, M. R. Chua, T. G. Park, Y. Lu, F. Rotermund, Y.-K. Kim, C. S. Moon, N. J. Jeon, J.-P. Correa-Baena, V. Bulović, S. S. Shin, M. G. Bawendi, J. Seo, *Nature* **2021**, 590, 587; c) K. Wang, C. Wu, Y. Hou, D. Yang, T. Ye, J. Yoon, M. Sanghadasa, S. Priya, *Energy & Environmental Science* **2020**, 13, 3412; d) C. Ran, W. Gao, J. Li, J. Xi, L.

Li, J. Dai, Y. Yang, X. Gao, H. Dong, B. Jiao, I. Spanopoulos, C. D. Malliakas, X. Hou, M. G. Kanatzidis, Z. Wu, *Joule* **2019**, 3, 3072.

[9] a) H. Zhang, Z. Chen, M. Qin, Z. Ren, K. Liu, J. Huang, D. Shen, Z. Wu, Y. Zhang, J. Hao, C.-s. Lee, X. Lu, Z. Zheng, W. Yu, G. Li, *Advanced Materials* **2021**; b) N. Li, Z. Zhu, C.-C. Chueh, H. Liu, B. Peng, A. Petrone, X. Li, L. Wang, A. K.-Y. Jen, *Advanced Energy Materials* **2017**, 7, 1601307; c) S. Wu, J. Zhang, Z. Li, D. Liu, M. Qin, S. H. Cheung, X. Lu, D. Lei, S. K. So, Z. Zhu, A. K.-Y. Jen, *Joule* **2020**, 4, 1248.

[10] a) S. Tan, I. Yavuz, M. H. Weber, T. Huang, C.-H. Chen, R. Wang, H.-C. Wang, J. H. Ko, S. Nuryyeva, J. Xue, Y. Zhao, K.-H. Wei, J.-W. Lee, Y. Yang, *Joule* **2020**, 4, 2426; b) S. Masi, A. F. Gualdrón-Reyes, I. Mora-Seró, *ACS Energy Lett.* **2020**, 5, 1974; c) Y. Zhang, Z. Zhou, F. Ji, Z. Li, G. Cui, P. Gao, E. Oveisi, M. K. Nazeeruddin, S. Pang, *Advanced Materials* **2018**, 30, 1707143; d) M. L. Davies, *Joule* **2020**, 4, 1626.

[11] a) H. Z. Lu, Y. H. Liu, P. Ahlawat, A. Mishra, W. R. Tress, F. T. Eickemeyer, Y. G. Yang, F. Fu, Z. W. Wang, C. E. Avalos, B. I. Carlsen, A. Agarwalla, X. Zhang, X. G. Li, Y. Q. Zhan, S. M. Zakeeruddin, L. Emsley, U. Rothlisberger, L. R. Zheng, A. Hagfeldt, M. Gratzel, *Science* **2020**, 370, 74; b) C. H. Chen, Y. H. Lou, K. L. Wang, Z. H. Su, C. Dong, J. Chen, Y. R. Shi, X. Y. Gao, Z. K. Wang, *Advanced Energy Materials* **2021**, 2101538; c) H. Zhang, M. Qin, Z. Chen, W. Yu, Z. Ren, K. Liu, J. Huang, Y. Zhang, Q. Liang, H. T. Chandran, P. W. K. Fong, Z. Zheng, X. Lu, G. Li, *Advanced Materials* **2021**, 33, 2100009; d) M. Kim, G. H. Kim, T. K. Lee, I. W. Choi, H. W. Choi, Y. Jo, Y. J. Yoon, J. W. Kim, J. Lee, D. Huh, H. Lee, S. K. Kwak, J. Y. Kim, D. S. Kim, *Joule* **2019**, 3, 2179; e) H. X. Dang, K. Wang, M. Ghasemi, M. C. Tang, M. De Bastiani, E. Aydin, E. Duzon, D. Barrit, J. Peng, D. M. Smilgies, S. De Wolf, A. Amassian, *Joule* **2019**, 3, 1746.

[12] a) Y. Rong, Z. Tang, Y. Zhao, X. Zhong, S. Venkatesan, H. Graham, M. Patton, Y. Jing, A. M. Guloy, Y. Yao, *Nanoscale* **2015**, 7, 10595; b) T. Bu, J. Li, H. Li, C. Tian, J. Su, G. Tong, L. K. Ono, C. Wang, Z. Lin, N. Chai, X.-L. Zhang, J. Chang, J. Lu, J. Zhong, W. Huang, Y. Qi, Y.-B. Cheng, F. Huang, *Science* **2021**, 372, 1327; c) N. J. Jeon, J. H. Noh, Y. C. Kim, W. S. Yang, S. Ryu, S. I. Seok, *Nat Mater* **2014**, 13, 897; d) C. C. Boyd, R. C. Shallcross, T. Moot, R. Kerner, L. Bertoluzzi, A. Onno, S. Kavadiya, C. Chosy, E. J. Wolf, J. Werner, J. A. Raiford, C. de Paula, A. F. Palmstrom, Z. S. J. Yu, J. J. Berry, S. F. Bent, Z. C. Holman, J. M. Luther, E. L. Ratcliff, N. R. Armstrong, M. D. McGehee, *Joule* **2020**, 4, 1759.

[13] a) Y. H. Deng, C. H. Van Brackel, X. Z. Dai, J. J. Zhao, B. Chen, J. S. Huang, *Sci Adv* **2019**, 5; b) N. Ahn, D. Y. Son, I. H. Jang, S. M. Kang, M. Choi, N. G. Park, *J Am Chem Soc* **2015**, 137, 8696; c) Y. Chen, S. Tan, N. Li, B. Huang, X. Niu, L. Li, M. Sun, Y. Zhang, X. Zhang, C. Zhu, N. Yang, H. Zai, Y. Wu, S. Ma, Y. Bai, Q. Chen, F. Xiao, K. Sun, H. Zhou, *Joule* **2020**, 4, 1961.

[14] a) S. Sanchez, L. Pfeifer, N. Vlachopoulos, A. Hagfeldt, *Chem Soc Rev* **2021**; b) Y. M. Xie, Q. Xue, H. L. Yip, *Advanced Energy Materials* **2021**; c) M. Qin, H. Xue, H. Zhang, H. Hu, K. Liu, Y. Li, Z. Qin,

J. Ma, H. Zhu, K. Yan, G. Fang, G. Li, U. S. Jeng, G. Brocks, S. Tao, X. Lu, *Advanced Materials* **2020**, 32, 2004630; d) Y. Yang, H. Lu, S. Feng, L. Yang, H. Dong, J. Wang, C. Tian, L. Li, H. Lu, J. Jeong, S. M. Zakeeruddin, Y. Liu, M. Grätzel, A. Hagfeldt, *Energy & Environmental Science* **2021**; e) Z. L. Li, A. Johnston, M. Y. Wei, M. I. Saidaminov, J. M. de Pina, X. P. Zheng, J. K. Liu, Y. Liu, O. M. Bakr, E. H. Sargent, *Joule* **2020**, 4, 631; f) S. Rayishankar, S. Gharibzadeh, C. Roldan-Carmona, G. Grancini, Y. Lee, M. Ralaiarisoa, A. M. Asiri, N. Koch, J. Bisquert, M. K. Nazeeruddin, *Joule* **2018**, 2, 788; g) F. H. Isikgor, F. Furlan, J. Liu, E. Ugur, M. K. Eswaran, A. S. Subbiah, E. Yengel, M. De Bastiani, G. T. Harrison, S. Zhumagali, C. T. Howells, E. Aydin, M. Wang, N. Gasparini, T. G. Allen, A. u. Rehman, E. Van Kerschaver, D. Baran, I. McCulloch, T. D. Anthopoulos, U. Schwingenschlögl, F. Laquai, S. De Wolf, *Joule* **2021**, 5, 1566.

[15] a) Y. Bai, S. Xiao, C. Hu, T. Zhang, X. Meng, Q. Li, Y. Yang, K. S. Wong, H. Chen, S. Yang, *Nano Energy* **2017**, 34, 58; b) S. Wang, J. Jin, Y. Qi, P. Liu, Y. Xia, Y. Jiang, R. X. He, B. Chen, Y. Liu, X. Z. Zhao, *Advanced Functional Materials* **2020**, 30, 1908343; c) J. Li, R. Munir, Y. Fan, T. Niu, Y. Liu, Y. Zhong, Z. Yang, Y. Tian, B. Liu, J. Sun, D.-M. Smilgies, S. Thoroddsen, A. Amassian, K. Zhao, S. F. Liu, *Joule* **2018**, 2, 1313; d) J. H. Zhang, Z. W. Wang, A. Mishra, M. L. Yu, M. Shasti, W. Tress, D. J. Kubicki, C. E. Avalos, H. Z. Lu, Y. H. Liu, B. I. Carlsen, A. Agarwalla, Z. S. Wang, W. C. Xiang, L. Emsley, Z. H. Zhang, M. Gratzel, W. L. Guo, A. Hagfeldt, *Joule* **2020**, 4, 507; e) E. Aydin, M. De Bastiani, S. De Wolf, *Adv Mater* **2019**, 31, e1900428.

[16] a) L. Zhu, X. Zhang, M. Li, X. Shang, K. Lei, B. Zhang, C. Chen, S. Zheng, H. Song, J. Chen, *Advanced Energy Materials* **2021**, 11; b) Q. Hu, W. Chen, W. Q. Yang, Y. Li, Y. C. Zhou, B. W. Larson, J. C. Johnson, Y. H. Lu, W. K. Zhong, J. Q. Xu, L. Klivansky, C. Wang, M. Salmeron, A. B. Djurisić, F. Liu, Z. B. He, R. Zhu, T. P. Russell, *Joule* **2020**, 4, 1575; c) M. Kim, I. W. Choi, S. J. Choi, J. W. Song, S. I. Mo, J. H. An, Y. Jo, S. Ahn, S. K. Ahn, G. H. Kim, D. S. Kim, *Joule* **2021**, 5, 659; d) A. R. B. Mohd Yusoff, M. Vasilopoulou, D. G. Georgiadou, L. C. Palilis, A. Abate, M. K. Nazeeruddin, *Energy & Environmental Science* **2021**, 14, 2906; e) W. C. Huang, T. L. Bu, F. Z. Huang, Y. B. Cheng, *Joule* **2020**, 4, 975; f) R. Wang, J. J. Xue, L. Meng, J. W. Lee, Z. P. Zhao, P. Y. Sun, L. Cai, T. Y. Huang, Z. X. Wang, Z. K. Wang, Y. Duan, J. L. Yang, S. Tan, Y. Yuan, Y. Huang, Y. Yang, *Joule* **2019**, 3, 1464; g) B. Chen, P. N. Rudd, S. Yang, Y. Yuan, J. Huang, *Chem Soc Rev* **2019**, 48, 3842.

[17] a) S. P. Dunfield, L. Bliss, F. Zhang, J. M. Luther, K. Zhu, M. F. A. M. Hest, M. O. Reese, J. J. Berry, *Advanced Energy Materials* **2020**, 10, 1904054; b) S. M. Yoon, H. Min, J. B. Kim, G. Kim, K. S. Lee, S. I. Seok, *Joule* **2021**, 5, 183; c) E. B. Bi, W. T. Tang, H. Chen, Y. B. Wang, J. Barbaud, T. H. Wu, W. Y. Kong, P. Tu, H. Zhu, X. Q. Zeng, J. J. He, S. Kan, X. D. Yang, M. Gratzel, L. Y. Han, *Joule* **2019**, 3, 2748; d) D. Luo, R. Su, W. Zhang, Q. Gong, R. Zhu, *Nature Reviews Materials* **2020**, 5, 44.

[18] N. X. Li, Y. Q. Luo, Z. H. Chen, X. X. Niu, X. Zhang, J. Z. Lu, R. Kumar, J. K. Jiang, H. F. Liu, X. Guo, B. Lai, G. Brocks, Q. Chen, S. X. Tao, D. P. Fenning, H. P. Zhou, *Joule* **2020**, 4, 1743.



- [19] a) T. A. S. Doherty, S. Nagane, D. J. Kubicki, Y.-K. Jung, D. N. Johnstone, A. N. Iqbal, D. Guo, K. Frohna, M. Danaie, E. M. Tennyson, S. Macpherson, A. Abfalterer, M. Anaya, Y.-H. Chiang, P. Crout, F. S. Ruggeri, S. Collins, C. P. Grey, A. Walsh, P. A. Midgley, S. D. Stranks, *Science* **2021**, 374, 1598; b) X. Zheng, C. Wu, S. K. Jha, Z. Li, K. Zhu, S. Priya, *ACS Energy Lett.* **2016**, 1, 1014.
- [20] D. Luo, W. Yang, Z. Wang, A. Sadhanala, Q. Hu, R. Su, R. Shivanna, G. F. Trindade, J. F. Watts, Z. Xu, T. Liu, K. Chen, F. Ye, P. Wu, L. Zhao, J. Wu, Y. Tu, Y. Zhang, X. Yang, W. Zhang, R. H. Friend, Q. Gong, H. J. Snaith, R. Zhu, *Science* **2018**, 360, 1442.
- [21] H. Shan, W. Xuan, Z. Li, D. Hu, X. Gu, S. Huang, *ACS Appl. Nano Mater.* **2022**, 5, 6801.
- [22] H. Su, J. Zhang, Y. Hu, X. Du, Y. Yang, J. You, L. Gao, S. Liu, *Advanced Energy Materials* **2021**, 11, 2101454.

**Synergistic Crystallization and Passivation by A Single Molecular Additive for High Performance Perovskite Solar Cells**

*Xinyi Du<sup>a</sup>, Jing Zhang<sup>a,\*</sup>, Hang Su<sup>a,b</sup>, Xu Guo<sup>a</sup>, Yingjie Hu<sup>a</sup>, Dongle Liu<sup>a</sup>, Ningyi Yuan<sup>c</sup>, Jianning Ding<sup>c</sup>, Lili Gao<sup>a,\*</sup>, Shengzhong (Frank) Liu<sup>a,b,\*</sup>*

By simultaneous control of the intermediate phase during crystallization of the perovskite film and surface passivation using the molecule DIAI with multiple functional groups, this strategy enabled us to obtain an impressive device PCE as high as 24.13% with negligible hysteresis. The bare device without any encapsulation maintains 94.1% of its initial efficiency after ambient exposure for over 1000 hours.

ToC figure

